Biophysical *Journal*
Article

Biophysical Society

Mechanical Model of Nuclei Ordering in *Drosophila* Embryos Reveals Dilution of Stochastic Forces

Franz Kaiser,[1] Zhiyi Lv,[2] Daniel Marques Rodrigues,[2] Jan Rosenbaum,[3] Timo Aspelmeier,[3] Jörg Großhans,[2] and Karen Alim[1,*]

[1]Biological Physics and Morphogenesis Group, Max Planck Institute for Dynamics and Self-Organization, Göttingen, Germany; [2]Institute for Developmental Biochemistry, Medical School, University of Göttingen, Göttingen, Germany; and [3]Institute for Mathematical Stochastics and Felix-Bernstein-Institute for Mathematical Statistics in the Biosciences, University of Göttingen, Göttingen, Germany

ABSTRACT During the initial development of syncytial embryos, nuclei go through cycles of nuclear division and spatial rearrangement. The arising spatial pattern of nuclei is important for subsequent cellularization and morphing of the embryo. Although nuclei are contained within a common cytoplasm, cytoskeletal proteins are nonuniformly packaged into regions around every nucleus. In fact, cytoskeletal elements like microtubules and their associated motor proteins exert stochastic forces between nuclei, actively driving their rearrangement. Yet, it is unknown how the stochastic forces are balanced to maintain nuclear order in light of increased nuclear density upon every round of divisions. Here, we investigate the nuclear arrangements in *Drosophila melanogaster* over the course of several nuclear divisions starting from interphase 11. We develop a theoretical model in which we distinguish long-ranged passive forces due to the nuclei as inclusions in the elastic matrix, namely the cytoplasm, and active, stochastic forces arising from the cytoskeletal dynamics mediated by motor proteins. We perform computer simulations and quantify the observed degree of orientational and spatial order of nuclei. Solely doubling the nuclear density upon nuclear division, the model predicts a decrease in nuclear order. Comparing results to experimental recordings of tracked nuclei, we make contradictory observations, finding an increase in nuclear order upon nuclear divisions. Our analysis of model parameters resulting from this comparison suggests that overall motor protein density as well as relative active-force amplitude has to decrease by a factor of about two upon nuclear division to match experimental observations. We therefore expect a dilution of cytoskeletal motors during the rapid nuclear division to account for the increase in nuclear order during syncytial embryo development. Experimental measurements of kinesin-5 cluster lifetimes support this theoretical finding.

INTRODUCTION

Active self-organization appears over a broad range of biological systems (1). Although the main focus was on pattern formation as self-organization on large, supercellular scales during the last century (2–4), more recent approaches also focus on inter- and intracellular interaction (5), taking into account individual cellular components. As such, the active dynamics of cytoskeletal building blocks like actin-filaments and microtubules emerged as an important part of self-organization and functioning on the cellular level (6,7). For example, forces generated from myosin motor proteins progressing on actin-filaments are now known to be crucial for the control of cell shape and morphogenesis (8–10). Yet, because of random binding and unbinding events of motors participating in the cytoskeletal dynamics, the forces generated are stochastic and can counteract overall ordered arrangements.

The action of cytoskeletal forces and the impact of their stochastic nature is underlying the spatial patterning of nuclei within syncytial embryos, specifically those studied in *Drosophila melanogaster* (11). Early *Drosophila* embryos form a syncytium up to nuclear cycle 14. During this stage, nuclei are embedded within a common cytoplasm without individual cell compartments (12). In nuclear cycles 10–13, nuclei form a two-dimensional array constrained to the embryo surface, where the dynamics of their rearrangements can be studied with common microscopy techniques. Nuclear rearrangement is driven by forces generated from cytoskeletal elements. In general, actin filaments and microtubules along with their associated motor proteins form a large network spanning the entire embryo. Yet, despite the common cytoplasm, the cytoskeleton is not uniform. Instead, each nucleus is additionally surrounded by a basket of microtubules (13) connected to the centrosomes and

Submitted August 21, 2017, and accepted for publication February 5, 2018.

*Correspondence: karen.alim@ds.mpg.de

Editor: Stanislav Shvartsman.

https://doi.org/10.1016/j.bpj.2018.02.018

associated with an F-actin cap (14–19) anchoring the nucleus in the embryo cortex; see Fig. 1. Overlapping microtubule baskets result in internuclear forces probably mediated by motor proteins (11,14,15,20). The actin caps most likely stabilize the nuclear positions but could in principle also modify the properties of the cytoplasm through a response mechanism (11,14,21). Because motor proteins randomly bind and unbind from microtubules, this repulsive force due to the overlap of microtubule baskets is very stochastic in nature; see Fig. 1 *d*. A balance between all forces arising from surrounding and nucleus-centered cytoskeletal elements organizes the nuclear arrangement within the embryo during the syncytial stage. During interphase 14, nuclei are cellularized by membranes forming between nuclei, and then gastrulation starts (12). Ordered nuclei arrangements are important for successful cellularization.

To establish ordered nuclear arrangements, the stochastic force arising from the microtubule dynamics has to be tamed. In particular, the increase in nuclear density during mitosis could naively be expected to coincide with an increase in stochastic activity, resulting in less-ordered nuclei. Theoretical models so far have mainly focused on mitosis itself, motivated by the fact that nuclear divisions in cycles 10–13 happen in waves usually starting simultaneously from the anterior and posterior poles of the embryo (12). Recent models describe the mitotic wave as a result of the embryo being a mechanically excitable medium (22), within the dynamics of Cdk1 activity (23), or make use of individual nuclear ages (15) to account for the observed synchronous propagation in mitosis. Yet, the reordering of nuclei after mitosis is only described explicitly in the latter model, namely by deterministic and potentially repulsive or attractive internuclear forces.

Here, we investigate the nuclear arrangements in *Drosophila* during interphases following the embryo throughout nuclear cycles 11–13. We develop a mechanical model of nuclei positioning considering passive and active forces. Passive forces arise due to the nuclei acting as force dipoles embedded in the cytoplasm and long-ranged cytoskeletal elements spanning the embryo. They are distinct from active, stochastic forces generated by overlapping microtubule baskets being pushed apart by motor proteins. To model the passive forces, we describe the nuclei as inclusions within an elastic matrix motivated by models for cell arrangements (24–27). The active force is described as an internuclear force with a constant activity time but a stochastic on-rate of a determined frequency to model the microtubule motor processivity and hopping rate. We perform computer simulations of the mechanical model, quantify the observed degree of orientational and spatial order, and relate the results to the model parameters. In addition, we follow experimental recordings of nuclear order and identify corresponding model parameters from comparison with the observed quantitative measures of nuclear order. Our findings suggest that simply doubling the number of nuclei in simulations cannot account for the changes in order arising due to mitosis because average nuclear order decreases in experiments, although it increases in

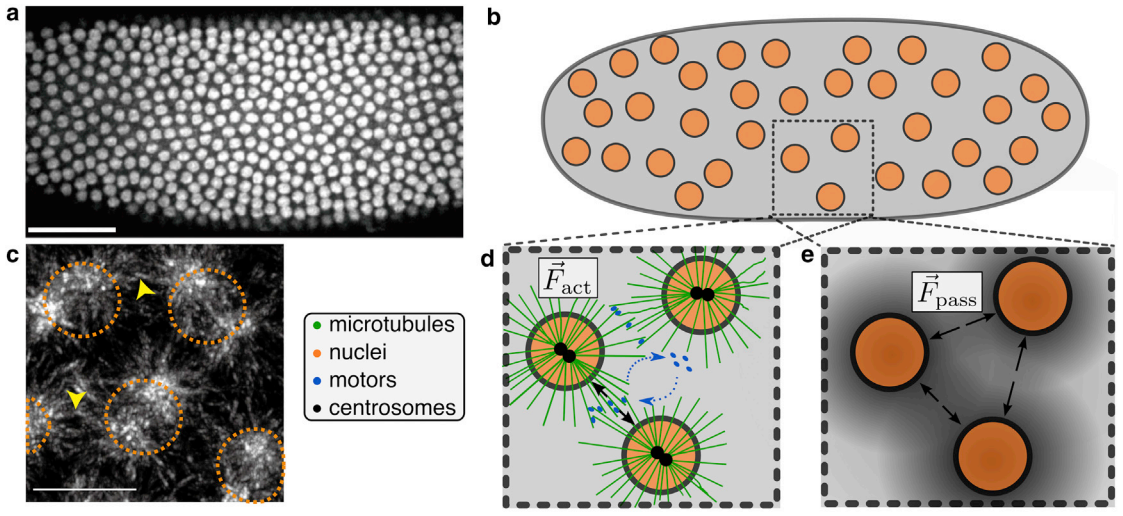

FIGURE 1 (*a*) Live image of *Drosophila* embryo expressing histone H2Av-GFP (*gray*) in interphase 13. Scale bars, 50 μm. (*b*) A schematic drawing of nuclei in the embryo is shown: interaction between nuclei (*orange*) through active forces (*d*) and passive forces (*e*) drives nuclear rearrangement. (*c*) A live image of a *Drosophila* embryo expressing EB1-GFP, which labels the growing tips of microtubules, is shown in interphase 13. Microtubule asters are shown by a temporal projection of EB1-GFP in 50s. The nuclear position is marked by the orange dashed line. Microtubules of neighboring nuclei overlap (*yellow arrows*). Scale bars, 5 μm. (*d*) A schematic representation of (*c*) is shown: microtubule baskets (*green*) anchored at centrosomes (*black dots*) of neighboring nuclei may overlap, and motors (*blue*) may hop on and off (*blue*, *dotted arrows*) of overlapping microtubules. Motors slide microtubule filaments of neighboring nuclei apart and thus produce an active, stochastic interaction force $\vec{F}_{\mathrm{act}}$ that acts repulsively (*black arrows*). (*e*) In addition to the stochastic forcing, nuclei (*orange circles*) present inclusions in an elastic matrix and interact with each other through their deformations of the matrix (*shaded black region*), resulting in a passive interaction force $\vec{F}_{\mathrm{pass}}$ that acts repulsively as well (*black arrows*). To see this figure in color, go online.

simulations. Instead, we find that reducing the model parameters corresponding to the motor protein activity together with doubling the number of nuclei in the simulated system reproduces the nuclear order observed in experiment. Thus, our findings suggest that stochastic forces are diluted as motor density stays fixed during the rapid nuclear divisions. This theoretical prediction is in agreement with motor cluster lifetime measurements of microtubules during *Drosophila* development.

MATERIALS AND METHODS

Mechanical model of nuclei ordering

We model nuclear ordering as the result of two interactions. The first interaction takes the form of passive forces based on the interaction of nuclei within an elastic matrix modeling the shared cytoplasm and the long-ranged cytoskeletal elements. The second interaction takes the form of active forces arising from motor-mediated microtubule repulsion between neighboring nuclei.

Passive forces mediated by an elastic matrix

Within the syncytial embryo, nuclei are embedded in a complex matrix composed of cytoplasm and cytoskeletal elements, giving rise to long-ranged interactions between nuclei. This is a similar setting to that of cells in soft materials, which have been shown to be successfully regarded as force dipoles interacting within an elastic matrix (24,25,27,28). We adapt the framework of Schwarz and Safran (24), originally derived for cells, to the setting of nuclei in a syncytial embryo by deriving the interaction potential of nuclei in a semiinfinite two-dimensional elastic space.

Consider the layer below the surface of the syncytial embryo, which is modeled as an elastic matrix with Lamé parameters μ and λ. This surface spans $\sim$40 μm up to the yolk in the center of the ellipsoidal embryo. Regarding the motion of nuclei within this elastic matrix, tangential force components dominate over normal components, resulting in nuclear displacements in the order of a few μm during interphase. Thus, displacements are small in comparison to the elastic matrix's extension, allowing nuclei to be modeled using the two-dimensional approximation of the *Boussinesq* problem (24,28). Nuclear movement is thus restricted to the two-dimensional plane of the embryo's surface. A nucleus within this matrix can for now be regarded as a passive inclusion that leads to a deformation $\vec{u}(\vec{r})$ at $\vec{r} = (x_1, x_2)$. In mechanical equilibrium, i.e., for $\partial_j \sigma_{ij}^{tot} = 0$, we can decompose the total stress $\sigma_{ij} = \sigma_{ij}^{\mathrm{el}} + \sigma_{ij}^{\mathrm{inc}}$ into an elastic part and a part that is generated because of the inclusion. Here, $i, j \in \{1, 2\}$ represent the components in the x_1 or x_2 direction. The latter part can be represented as $f_i = -\partial_j \sigma_{ij}^{\mathrm{inc}} = \partial_j \sigma_{ij}^{\mathrm{el}}$, a body force in the direction i acting on the elastic matrix. The deformation in direction i due to a single nucleus α is given by (29)

$$u_i^{\alpha}(\vec{r}) = \int_{A_\alpha} d^2 r' \sum_{j=1}^{2} G_{ij}(\vec{r} - \vec{r}') f_j^{\alpha}(\vec{r}'),$$

where A_α is the nucleus's area excluding microtubule baskets, and $G_{ij}(\vec{r} - \vec{r}')$ is the elastic Green's function, i.e., the displacement in direction i at point $\vec{r}$ due to a force in direction j at point $\vec{r}'$. For the setting introduced here of an isotropic, effectively two-dimensional medium, the Green's function reads (see e.g., (28,29, chapter 8)) as the following:

$$G_{ij}(\Delta\vec{r}) = \frac{1}{4\pi(\mu+\lambda)\Delta r}\left[2\delta_{ij} + \tfrac{\lambda}{\mu}\left(\delta_{ij} + \frac{\Delta x_j \Delta x_i}{(\Delta r)^2}\right)\right],$$

which introduces the difference vector $\Delta\vec{r} = (\Delta x_1, \Delta x_2) = \vec{r} - \vec{r}'$ with length $\Delta r = |\Delta\vec{r}|$. The strain resulting from the deformation is mediated by the matrix and can thus be felt by another inclusion and vice versa, leading to an effective interaction energy between two nuclei α and β:

$$\begin{aligned} W^{\alpha\beta} &= -\sum_{j=1}^{2} \int_{A_\alpha} d^2 r \; u_j^{\beta}(\vec{r}) f_j^{\alpha}(\vec{r}) \\ &= -\sum_{i,j=1,1}^{2,2} \int_{A_\alpha} d^2 r \int_{A_\beta} d^2 r' f_j^{\alpha}(\vec{r}) f_i^{\beta}(\vec{r}') G_{ij}(\vec{r}' - \vec{r}). \end{aligned}$$

We assume that nuclei cannot overlap, i.e., the two integration domains are two separate regions within the matrix with $A_\alpha \cap A_\beta = \varnothing$. For force distributions localized around a nucleus's center of mass $\vec{R}^{\alpha}$, we can expand the interaction energy using a multipole expansion, which yields to lowest order:

$$\begin{aligned} W^{\alpha\beta} &= -\sum_{j=1}^{2} \int_{A_\alpha} d^2 r' u_j^{\beta}\left(\vec{R}^{\alpha} + \vec{r}'\right) f_j^{\alpha}(\vec{r}') \\ &= -\sum_{j=1}^{2} \int_{A_\alpha} d^2 r' f_j^{\alpha}(\vec{r}') \sum_{k=0}^{\infty} \frac{\left(\left(\vec{R}^{\alpha} + \vec{r}'\right)\vec{\nabla}\right)^k}{k!} u_j^{\beta}\left(\vec{R}^{\alpha} + \vec{r}'\right) \\ &\approx -\sum_{i,j=1,1}^{2,2} P_{ij} \partial_i' u_j^{\beta}\left(\vec{R}^{\alpha}\right) \end{aligned}$$

where the monopoles $Q_j = \int_A d^2 r f(r)(x_j/r)$ vanish because of the antisymmetry of the corresponding expression, and we defined the force dipoles $P_{ij} = \int_A d^2 r f(r)(x_j x_i/r) = P\delta_{ij}$ assuming that $f_j(r) = (x_j/r) f(r)$ and circular nuclei. In more general cases, the monopole contribution can be neglected using $\sum_j Q_j = 0$ (25).

Along the same lines, we can expand the interaction energy to second order in terms of the other nucleus's center of mass $\vec{R}^{\beta}$, which leads to the following:

$$\begin{aligned} W^{\alpha\beta} &= \sum_{i,j=1,1}^{2,2} P^2 \partial_i \partial_j G_{ij}(\Delta\vec{x}_{\alpha\beta}) \\ &= P^2 \frac{K}{4\pi\mu} \frac{1}{\Delta r_{\alpha\beta}^3}, \end{aligned}$$

where $K = (\lambda + 2\mu/\lambda + \mu)$, and $\Delta\vec{x}_{\alpha\beta} = \vec{R}^{\beta} - \vec{R}^{\alpha}$ denotes the distance vector between both interacting nuclei with length $\Delta r_{\alpha\beta} = |\Delta\vec{x}_{\alpha\beta}|$. This potential results in the following passive interaction force by nucleus β on nucleus α:

$$\vec{F}_{\mathrm{pass},\alpha\beta}(\Delta\vec{x}) = -\vec{\nabla}^{\alpha} W^{\alpha\beta} = -\widehat{F}_{\mathrm{pass}} \frac{\Delta\vec{x}_{\alpha\beta}}{\Delta r_{\alpha\beta}^5}, \qquad (1)$$

where $\widehat{F}_{\mathrm{pass}} = 3P^2(K/4\pi\mu)$ is the passive force's amplitude.

Active forces arising from motor processivity on overlapping microtubule baskets

In addition to the passive forces due to the nuclei being embedded in an elastic matrix, active, stochastic forces arise when microtubule baskets of neighboring nuclei overlap. Headed motor proteins, such as kinesin-5, bind two microtubules of both baskets and while walking on them generate

an active force that persists as long as the motor protein is bound (30). Overlapping baskets have been observed to result in both repulsive and attractive interactions. In principle, either attractive or repulsive forces between nuclei could both stabilize nuclear order. Because so far mainly repulsive forces were observed in wild-type embryos (11,14), we confine our analysis to this case. We model the active force exerted by nucleus β on nucleus α as a function decaying with internuclear distances $\Delta r_{\alpha\beta}^{6}$. We choose a continuum model approach here to allow for an analytically tractable model of active inclusions motivated by (31) in future work. To incorporate the short-ranged character of active interactions between overlapping microtubule baskets, we numerically cut off interactions after distances of three times the system-averaged nearest-neighbor distance $\langle r_{nn}\rangle$; see Numerical Simulation of Nuclei Arrangements Matching Initial Condition from Data for details. Individual forces are turned on stochastically and last for time τ, which represents the average processivity time of a motor bound to overlapping microtubules as follows:

$$\vec{F}_{\mathrm{act},\alpha\beta}(\Delta\vec{x},t) \;=\; -\widehat{F}_{\mathrm{act}}\frac{\Delta\vec{x}_{\alpha\beta}}{\Delta r_{\alpha\beta}^{6}}\sum_{t_k}\overline{\Theta}(t,t_k), \tag{2}$$

where $\overline{\Theta}(t,t_k)=\Theta(t-t_k)\Theta(t_k+\tau-t)$ only assumes nonzero values for $t\in\{t_k,\,t_k+\tau\}$. We assume the motor processivity time τ to be constant over system and time. The stochastic nature of this active interaction only enters by the random onset times of interactions, t_k. Given the large system size, we assume that the overall number of active forces acting in the whole system at a given time point does not vary a lot over the course of one interphase. For this reason, we define a frequency-like parameter $p\in[0,1]$ as the time-averaged ratio of the number of active forces actually acting in the system to the number of possible interactions. Finally, $\widehat{F}_{\mathrm{act}}$ is the active force's amplitude. Because the active force is more short-ranged than the passive force, we chose a faster decay with internuclear distance, $(\vec{x}/r^6)$-dependence, rather than the $(\vec{x}/r^5)$-dependence in $\vec{F}_{\mathrm{pass}}$. That said, model results are robust against changes to the dependence on internuclear distance (see Fig. S2).

Nuclei follow overdamped dynamics in small parameter space

Within the syncytial embryo, nuclei are moving in a viscous medium $\eta\approx 1.0\,\mathrm{kg/(s\cdot m)}$ (32) at roughly the density of water $\rho\approx 1\cdot 10^{3}\,\mathrm{kg/m^{3}}$, only moving with velocities of about $U\approx 2\cdot 10^{-6}\,\mathrm{m/min}$ while having a diameter of $D\approx 5\cdot 10^{-6}\,\mathrm{m}$ for the interphases considered here (33). Thus, the ratio of inertial to viscous forces is small, as exemplified by the small Reynolds number $\mathrm{Re}=(UD\rho/\eta)\approx 10^{-10}$. The motion of a nucleus α at position $\vec{r}_\alpha$ is therefore well described by the following overdamped equation of motion:

$$\begin{aligned}\dot{\vec{r}}_\alpha(t) \;&=\; \tfrac{1}{\eta}\sum_{\beta\neq\alpha}^{N}\left(\vec{F}_{\mathrm{pass},\alpha\beta}(\Delta\vec{x})+\vec{F}_{\mathrm{act},\alpha\beta}(\Delta\vec{x},t)\right)\\ &=\; -\frac{1}{\eta}\sum_{\beta\neq\alpha}\frac{\Delta\vec{x}_{\alpha\beta}}{\Delta r_{\alpha\beta}^{5}}\left(\widehat{F}_{\mathrm{pass}}+\frac{\widehat{F}_{\mathrm{act}}}{\Delta r_{\alpha\beta}}\right)\sum_{t_k}\overline{\Theta}(t,t_k)).\end{aligned} \tag{3}$$

We introduce rescaled variables by defining dimensionless space $\vec{r}^{\,*}=\vec{r}/\langle r_{nn}\rangle$ (where $\langle r_{nn}\rangle$ is the system-averaged nearest-neighbor distance) and by rescaling time by $t^{*}=t/(\eta\cdot\langle r_{nn}\rangle)$, the active force's amplitude by $\widehat{F}^{*}_{\mathrm{act}}=\widehat{F}_{\mathrm{act}}/\langle r_{nn}\rangle^{5}$, and the passive force's amplitude by $\widehat{F}^{*}_{\mathrm{pass}}=\widehat{F}_{\mathrm{pass}}/\langle r_{nn}\rangle^{4}$, such that the amplitudes carry the dimension of forces. We identify four characteristic parameters that determine the dynamics of nuclei arrangement.

First, we consider the dimensionless ratio of force amplitudes $C=\widehat{F}^{*}_{\mathrm{pass}}/\widehat{F}^{*}_{\mathrm{act}}$, which represents the relative strength of the two forces. Higher values of C correspond to reduced stochastic force $\vec{F}_{\mathrm{act}}$ and thus can be expected to lead to more ordered nuclear arrangements. Secondly, we make use of the number of nuclei in the system N corresponding to the density ρ of nuclei per area. Thirdly, we use the percentage of stochastic forces acting within the nuclei ensemble over time p, which is again a measure of stochasticity in the system. We expect stochasticity to be maximal for intermediate values of p, i.e., for $p\approx 0.5$; because of the repulsive nature of both forces, an increase or decrease in p from 0.5 essentially has an ordering effect with the overall force being more regular in time. Finally, we include the motor processivity time in rescaled time units $\tau^{*}=\tau/(\eta\cdot\langle r_{nn}\rangle)$.

The degree of stochasticity is controlled by the time-averaged percentage of active motor sites across the entire nuclei ensemble p and the motor processivity τ. We found both parameters to affect nuclear arrangement in the same fashion, with p being much easier to tune in simulations performed; see Fig. S3. For this reason, we set τ to a constant value in the following sections and focus on the interplay of C, N, and p. Hereinafter, we will also omit the * notation and simply use the rescaled variables unless stated otherwise.

Quantifying spatial and orientational order across an embryo

To quantify nuclear order, we define measures for spatial and orientational order. Our characterization of orientational order is based on the concept of the hexagonal bond orientational parameter $\varphi_6(j)=1/n_j\sum_{i=1}^{n_j}e^{6i\theta_{ij}}$ originally introduced in (34). Here, n_j is the number of nearest neighbors of the object of interest j, and θ_{ij} is the angle between the line connecting the nearest neighbor i to particle j and a fixed reference axis such as the x axis. The hexagonal bond parameter classifies an entire arrangement by a value that varies between $\langle\varphi_6(j)\rangle=1$ for perfect hexagonal packing and $\langle\varphi_6(j)\rangle=0$ for a completely disordered system. The extension of the hexagonal bond orientational to the so-called hexatic correlation function, defined as $g_6(r)=\langle\varphi_6^{*}(i)\varphi_6(j)\delta(r-r_{ij})\rangle$ (34–36), inspired the following measure:

$$\begin{aligned}Z(r) \;&=\; \left\langle\varphi_6(i)\varphi_6^{*}(k)\Theta(r-r_{ik})\right\rangle\\ &=\; \frac{1}{N\cdot N(r)}\left|\sum_{i,k}^{N,N}\varphi_6(i)\varphi_6^{*}(k)\Theta(r-r_{ik})\right|.\end{aligned} \tag{4}$$

This parameter displays the spatial extension of significant ordering from the local hexagonal bond parameter retrieved for $r=0$ to the global order for very large r. Here, N is the total number of nuclei considered, $N(r)$ denotes the average number of nuclei within a disk of radius r, and r_{ik} is the Euclidean distance between object i and k; see Fig. 2. We integrate in space, obtaining the functional $\Theta(r-r_{ik})$ compared with the $\delta(r-r_{ik})$ dependence in the previous measure $g_6(r)$. This is more appropriate for active stochastic arrangements of objects in which no distinct peaks in hexatic correlation can be expected at characteristic distances. As we will compare nuclear arrangements of different densities, we refer to any spatial variable evaluated in r as normalized by the average nearest-neighbor nuclei distance $\langle r_{nn}\rangle$. Particularly characteristic for spatial decay in orientational order are $Z(r=1):=Z_0$ (i.e., the ensemble-averaged nearest-neighbor correlation of hexatic order) and the decay rate defined by the average gradient $\langle\nabla Z(r)\rangle_r$ and evaluated on a log-log scale to increase sensitivity.

Hexatic order parameters are designed to measure deviation from hexagonal order. Yet, active matter has been shown to be very sensitive in how it diverges from hexagonal order, which may be quantified using the number of neighbor distribution (37,38). In particular, the ratio of the frequency of objects with five neighbors f_5 and the frequency of those with seven neighbors f_7 is found to be discriminative (11):

$$Q_{5,7} \;=\; \frac{f_5}{f_7}.$$

This parameter can be expected to be bound to 1 as a lower limit for a realistic model of the embryo because this is the case for real embryos (11).

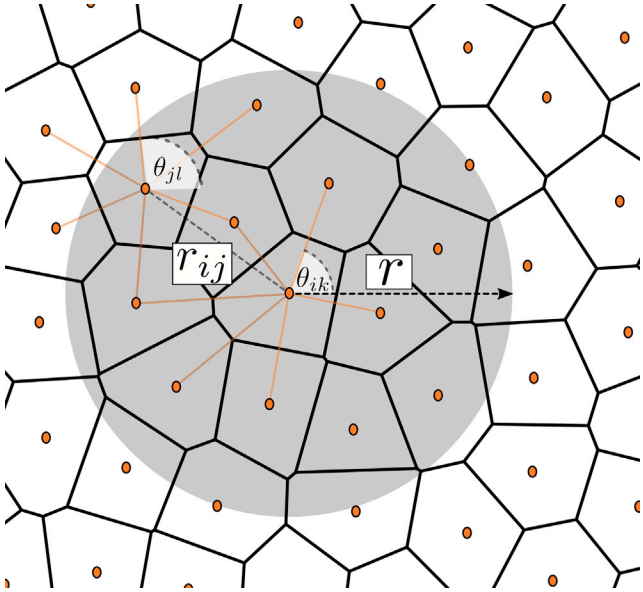

FIGURE 2 Schematic drawing to explain the order parameter $Z(r)$. The nearest neighbors of the nuclei (*orange circles*) are defined by adjacency in Voronoi tessellation (*black lines*). Exemplarily, two nuclei i and j are connected to their nearest neighbors through orange lines and to each other via a black dotted line, indicating their mutual distance r_{ij}. The corresponding angles between the lines connecting nuclei i and j with neighbors k and l, respectively, and a vector in the direction of the x axis as fixed reference axis have been marked by θ_{ik} and θ_{jl}, respectively. A perfect hexagonal arrangement corresponds to $\theta_{ik} = 60^\circ \ \forall i,k$. Spatial correlation in hexatic order is displayed by dependence on r in the order parameter $Z(r)$: given one nucleus i, all other nuclei within radius r are taken into account with the respective angles to their neighboring nuclei, as indicated here for nucleus j. The correlation in hexatic order, taking into account all nucleus-nucleus pairs within the shaded area, then denotes the order parameter. With disorder, the parameter will decay over r. To see this figure in color, go online.

With increasing order in nuclear arrangement, we expect this parameter to approach this lower limit because this corresponds to less asymmetries in the number of neighbors.

To quantify spatial order, we employ the radial distribution function of nuclei positions $g(r)$. Precisely, we quantify the value at the radial distribution function's first minimum r_1^*:

$$g\left(r = r_1^*\right).$$

We adopt the normalization condition $\int_0^5 g(r)dr = 1$, where r is the dimensionless rescaled radius, which we find to be more meaningful in the given context because of the limited system size. This parameter complements the order parameter $Z(r)$, allowing us to independently determine spatial and orientational order. The radial distribution function can be expected to have less pronounced peaks with increasing disorder, going from δ-peaks at maximal order, i.e., solid-like states, to a completely flat distribution for random arrangements, i.e., gas-like states, where fluid-likes states are characterized by intermediate relative peak sizes (39) (pp. 197). For this reason, we expect this parameter to decrease with increasing order in the arrangement. For completeness, we also tested for further measures of larger-scale order in liquid systems, so-called hyperuniformity (40). This concept is based on local density fluctuations and was found to be important in the context of many biological systems (see e.g., (41), Fig. S1).

Culturing and imaging of live *Drosophila* embryos

Genetic markers and strains are described in Flybase (42). The generation of the kinesin-5–green fluorescent protein (GFP) stock is described in (43). *Drosophila* embryos were dechorionated with hypochlorite for 90 s, washed with water, aligned on a piece of agar, transferred to a cover slip coated with glue, and covered with halocarbon oil (Voltalef 10S). Nuclear dynamics was recorded in embryos expressing His2Av-eGFP (11) with a Zeiss microscope (Carl Zeiss Microscopy, Jena, Germany) equipped with a spinning disc (25×/NA0.7 multiimmersion) with a frame rate of 2 or 5 s per frame. Four z sections covering a total of 8 μm were merged. Images of EB1-GFP (Fig. 1 *a*; (11)) and kinesin-5–GFP (Fig. 7) were recorded with a confocal microscope (Zeiss LSM780 with airy scan unit, 63×NA1.4/oil). The frame rate for kinesin-5 lifetime movies was 2/s.

The kinesin-5 images were taken at the apical position of the embryo where the astral microtubules localize. By lifetime of kinesin-5, we refer to the time that one kinesin-5–GFP cluster stays on astral microtubules. The counting of lifetime starts when one GFP cluster shows up between adjacent nuclei, and the counting ends when this cluster disappears, as shown in Fig. 7 *c*. Images were processed with Fiji/ImageJ (44).

Tracking nuclei in experimental recording

Identifying nuclei by blob detection

A video consists of a sequence of M frames. The nuclei were detected for each frame by using the blob detection algorithm described in (45). Briefly, this algorithm works as follows. Frame i for $i \in \{1, 2, \ldots, M\}$ is represented as a function f_i, with $f_i(x, y)$ being the grayscale value at position (x, y). The function f_i is convolved with Gaussian kernels $g_\sigma(x, y)$ with different variances σ^2, smoothing out details on scales smaller than σ. This results in a three-dimensional scale-space representation of the image with coordinates x, y and σ. For each σ, the Laplace Operator Δ is applied, and the result is scaled with a factor of σ^2, leading to

$$L_i(x, y, \sigma) := \sigma^2(\Delta(g_\sigma * f_i))(x, y, \sigma), \tag{5}$$

where * is the convolution operator. The locations $(x_{k,i}, y_{k,i}, \sigma_{k,i})$ of the local maxima of L_i correspond to points of high curvature and indicate blob-like features of size $\sigma_{k,i}$ at position $p_{k,i} = (x_{k,i}, y_{k,i})$, which we identify with the nuclei.

In some cases, more than one blob was found for a single nucleus, for example because the fluorescent light varied strongly inside a nucleus. Hence, if a blob shared more than 50% of its area with another blob, the blob with lower average value was disregarded.

Tracking nuclei trajectories over time

To extract trajectories of nuclei from the images, we needed to determine which nucleus in frame i corresponded to which nucleus in frame $i+1$. This was done using the following procedure. Denote the distance between nucleus k in frame i and nucleus l in frame $i+1$ by $d_{k,l,i} = \|n_{k,i} - n_{l,i+1}\|_2$. We identified a given nucleus k in frame i with a nucleus l in frame $i+1$ if their mutual distance $d_{k,l,i}$ was minimal with respect to l. If two nuclei k_1 and k_2 from frame i were identified with the same nucleus l in frame $i+1$ and, for example, $d_{k_1,l,i} < d_{k_2,l,i}$, we connected nucleus k_2 with its second-closest neighbor. This method was applied recursively for up to a maximal depth of eight, so a nucleus that would have to be connected to its ninth-closest neighbor was considered not to be connected at all.

Identifying mitosis

During mitosis, the SD of the distance between nearest neighbors normalized by the mean internuclear distance $\langle r_{nn} \rangle$ is known to show at least a

twofold increase (11). We use this robust criterion to identify mitosis and interphase in the recordings. Numerically identified time frames for interphase were subsequently confirmed by manual inspection of data. Nuclear order in interphase was analyzed using exactly the same numerics as that for simulated nuclear arrangements.

Numerical simulation of nuclei arrangements matching initial condition from data

To study the impact of active versus passive forces on nuclear arrangements, we performed numerical simulations of nuclei in a two-dimensional plane subject to the equations of motion in Eq. 3. Nuclei were placed on a square grid of dimensionless side length $G = 6.0$, employing periodic boundary conditions. Equations of motion were integrated in time using forward Euler steps of size $\mathrm{dt} = 10^{-5}$. The physical integration time was kept constant at $t_{\max} = 1.0$, i.e., the number of time steps was $N_t = 10^5$. Motor processivity τ was kept constant at 0.05 over all performed simulations, ensuring $\mathrm{dt} \ll \tau \ll t_{\max}$. Parameters p and C were varied between 0.1–0.9 and 0.25–2.0, respectively. The number of nuclei was varied between $N = 55, 108, 192$ with corresponding densities ρ_{11}, ρ_{12}, and ρ_{13}, where the index indicates the respective interphase to which the density corresponded. For initial conditions, we used nuclei positions tracked from extracts of experimental recordings corresponding to the respective number of nuclei, thereby matching the density of nuclei in both experiments and simulations.

The effective nearest-neighbor interaction in the active force was realized using a cutoff radius r_{cut} of approximately three system-averaged nearest-neighbor distances, such that nuclei that are not neighbors in the Voronoi sense may contribute to the interaction. Stochasticity in the active force was implemented as follows. Each individual internuclear interaction was based on a timer starting from τ that was decremented by dt for every time step in which the two nuclei interacted. That means that the interaction happened if the two nuclei were located within a distance of r_{cut} to one another and if their mutual timer was nonzero. Each timer that reached zero was reset to τ based on a threshold $k = p\,\mathrm{dt}/((1-p)\tau)$, depending on the system parameters p, dt, and τ. If a random number $k^* \in [0, 1]$ drawn from a uniform distribution was smaller than the threshold k, the interaction timer was reset to τ. That way, the overall percentage of active forces acting reached p on average.

When analyzing nuclear order, boundaries were treated as open boundaries. To determine the neighborhood relationship of nuclei, a Voronoi tessellation was performed based on nuclear positions. Nuclei sharing a common edge in the Voronoi tessellation were defined as nearest neighbors. When calculating nuclei order parameters, those nuclei were neglected whose Voronoi cells were not completely located within the complex hull of all nuclei. The radial distribution function was evaluated exclusively in the range $r \in [0.0, 5.0]$—because of the finite system size, resulting in a rapid decay of $g(r)$ with r—using bins of size $b = (1/10)$. The normalization condition $\int_0^5 g(r)dr = 1$ was adopted.

RESULTS

Order increases despite increase in nuclear density

To investigate how active, stochastic forces are balanced to maintain nuclear order in light of increased nuclear density upon every round of division, we tracked nuclei through several rounds of mitosis and compared observed nuclear order to simulation results. Fig. 3 displays a typical change in orientational order (Eq. 4) with radius $r/\langle r_{nn}\rangle$ for an embryo progressing through interphases 11, 12, and 13 (*left*) side-by-side with the model simulations with corresponding densities of nuclei (*right*). In the simulation, all parameters were kept constant except for the nuclei number, which roughly doubles between any subsequent interphases. When doubling the nuclear density, the stochastic force increased in the entire arrangement, thus decreasing order. In contrast to the simulation results, we observed that the time-averaged order parameter increased with subsequent interphases in the experimental data. Note that only data for small distances r are reliable as the finite number of nuclei induces large fluctuations at large r, as indicated by additional lines denoting the length of the shorter axis in the ellipsoidal embryo.

The increase in orientational order, as shown in Fig. 3, is consistent throughout independent data sets, reproduced in 12 out of 14 interphases compared in embryos,

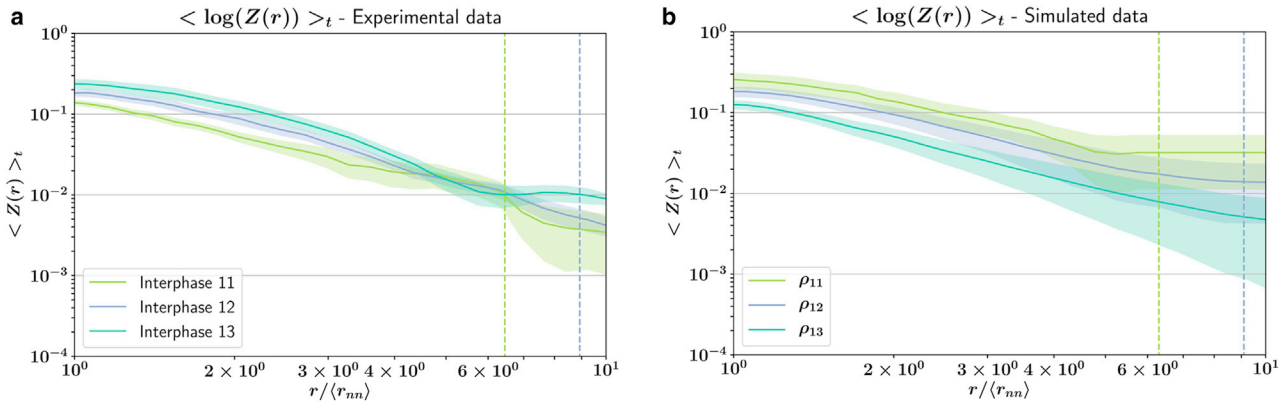

FIGURE 3 Orientational order increases with nuclear density in experimental data, contradicting the increase in stochastic force with the number of nuclei in the naive model. Orientational order parameter versus radius normalized by average nearest-neighbor distance on a log-log scale for experimental ((*a*), *left*) and simulated ((*b*), *right*) nuclear arrangement is shown. Exemplary data set showing how nuclear density progresses from ρ_{11} in interphase 11 (*light green curve*) via ρ_{12} in interphase 12 (*blue curve*) to ρ_{13} in interphase 13 (*dark green curve*). Shaded regions depict the SD over time. Dotted lines indicate the shorter axis of the ellipsoidal embryo, notifying insufficient significance at low nuclear count. Simulation parameters $\tau = 0.05$, $p = 0.4$, $C = 0.75$, and individual ρ are shown as indicated. To see this figure in color, go online.

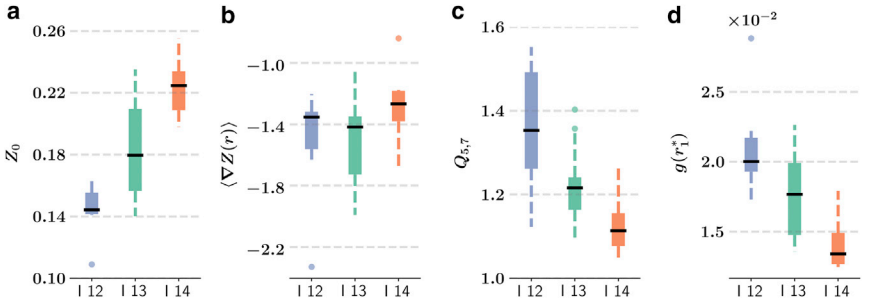

FIGURE 4 Order parameters averaged over 6 (interphase 12), 14 (interphase 13), and 8 (interphase 14) independently recorded embryos. Distribution of each parameter for interphases 12 (*left*, *blue*), 13 (*center*, *green*), and 14 (*right*, *red*) are shown. For Z_0 (*a*), an increase with subsequent interphases is observed in contrast to the observation in simulations, as indicated in Fig. 3, although there is no significant change in the average gradient $\langle \nabla Z(r) \rangle$ (*b*). $Q_{5,7}$ (*c*) and $g(r_1^*)$ (*d*) both display a decrease with subsequent interphases as well, indicating an increase in order. To see this figure in color, go online.

i.e., ≈85% of all data sets analyzed. We further quantified orientational and spatial order in all data sets by single parameter distributions; see Fig. 4. This confirmed that overall orientational order increased in subsequent interphases, exemplified by the ensemble-averaged nearest-neighbor correlation $Z_0 = Z(r = 1)$. Also, the radial decay of orientational order, depicted by the average slope $\langle \nabla Z(r) \rangle_r$, stayed roughly constant. Again, this is an observation contrary to an increase in stochasticity, which would display increased radial decay. The frequency of five neighbors over seven $Q_{5,7}$ decreases with doubling of nuclear content, as does the value of the radial distribution function evaluated at the first minimum $g(r_1^*)$. Therefore, all measures substantiate that order increases between subsequent interphases despite the doubling of nuclear density and thus the amount of potential microtubule basket overlap forming the basis of active, stochastic forces. We deduce that other physical properties within the embryo, represented by our remaining model parameters p and C, have changed with subsequent interphases buffering the potential increase in stochastic forces.

Stochastic force frequency and magnitude halved after mitosis

To explore how the average number of stochastic forces acting p and the ratio between passive and active force amplitude C affect disorder, we numerically sweep parameter space at a fixed density of interphase 13, ρ_{13}, and quantify all order parameters; see Fig. 5. Throughout all parameters, we observed that order increased with a decrease in stochasticity, i.e., higher weight on the passive forces by increasing C or a change in p to higher or lower values away from highest stochasticity at $p \approx 0.5$. Note

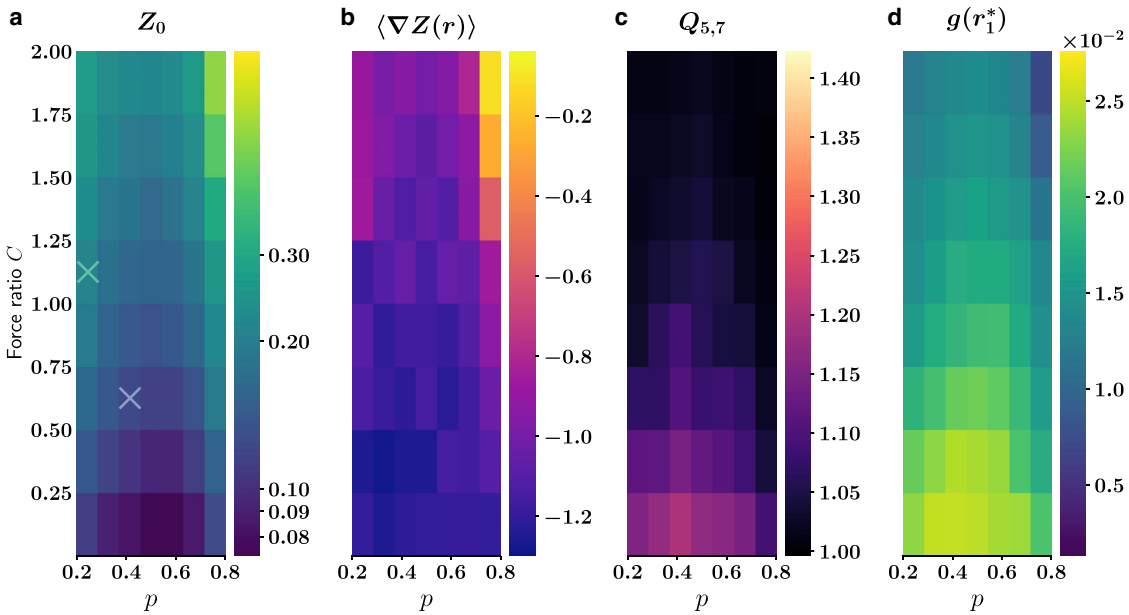

FIGURE 5 Change in orientational order parameters Z_0 (*a*), $\langle \nabla Z(r) \rangle$ (*b*), $Q_{5,7}$ (*c*), and spatial order parameter $g(r_1^*)$ (*d*) with model parameters. p on the abscissa denotes the average number of stochastic forces acting within the nuclei arrangement, and C on the ordinate indicates the ratio between passive and active force amplitude. The density of nuclei is kept constant at a value corresponding to interphase 13. Order generally increases when stochasticity is reduced by increasing C or driving p to lower or higher values than the state with highest fluctuations in active force $p = 0.5$. In (*a*), the points corresponding to the model parameters for interphase 12 (*blue cross*) and the corresponding model parameters adjusted to interphase 13 (*green cross*) are indicated. To see this figure in color, go online.

that parameter p is roughly symmetric at about $p \approx 0.5$ because oversaturating the stochastic forces above 0.5 will again give rise to more static force patterns, which also applies for less-active forces, i.e., $p < 0.5$. This is true because both passive and active forces act repulsively.

It is important to note that although all order parameters appear to be superficially correlated, the orientational order parameters Z_0 and $\langle \nabla Z(r) \rangle_r$ are in fact particularly distinct from $Q_{5,7}$ and $g(r_1^*)$. This is best visible by the extremum of the latter being shifted to lower values in p with respect to the former. This fact is crucial because it allows us to identify model parameter values p and C for interphase 13 by locating the experimentally observed order parameters within this parameter sweep. Similarly running a sweep at the nuclei density corresponding to interphase 12 enables us to observe how model parameter p and C would have to change to account for the experimentally observed change in order. By quantifying model parameters for the exemplary data set shown in Fig. 3, we find that whereas $C = 0.75$ and $p = 0.4$ are required to capture interphase 12's nuclear arrangement, the doubled nuclei at interphase 13 require $C = 1.25$ and $p = 0.2$; see Table 1. This change in parameters implies that both forms of stochasticity have been about halved. Surprisingly, the same argument holds for the adjustment of parameters for interphase 11. Simply changing model parameters by the same amount but in the opposite direction, going from $C = 0.75$ and $p = 0.4$ for interphase 12 to $C = 0.25$ and $p = 0.5$, results in comparable values in order parameters measured in experiment and simulation; see Table 1. This result is later confirmed with a parameter sweep for the nuclei density corresponding to interphase 11. Again, note that increasing p beyond $p = 0.5$ is futile because of the symmetry resulting in $p = 0.5$ as an upper bound for stochasticity. Fig. 6 shows the spatial dependence of the orientational order parameter $Z(r)$ with the revised model parameters, showing not only a qualitative but even a quantitative agreement with the experimentally observed order parameter. The disagreement between theory and experiment for high values of r is most likely due to the very limited system size, as only a small excerpt of the real system was used for simulations. This fact can presumably also account for the observed mismatch

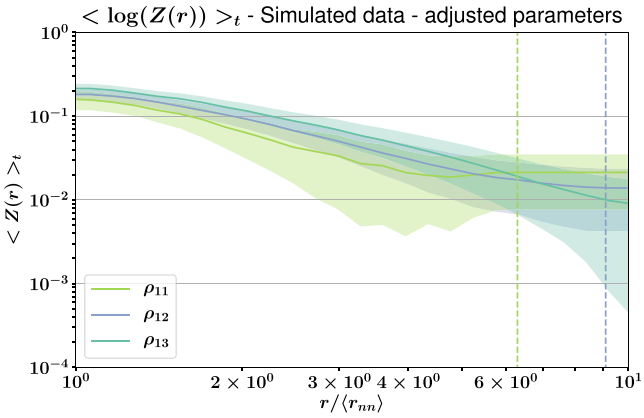

FIGURE 6 Orientational order parameter increases with nuclear density when, at the same time, stochasticity is halved. Simulations corresponding to interphase 13 (*dark green line*, *top*), interphase 12 (*blue line*, *center*), and interphase 11 (*light green line*, *bottom*) with shaded SD are shown. Stochasticity is reduced in underlying parameter values listed in Table 1. Dotted lines indicate a shorter axis of the ellipsoidal embryos, as obtained from analysis of experimental data sets. To see this figure in color, go online.

in the average gradient between experiment and theory $\langle \nabla Z(r) \rangle$.

A reduced stochasticity despite the potential increase in microtubule basket overlap suggests that the motor protein activity itself is reduced after mitosis, potentially affecting the force amplitude of the stochastic force $\widehat{F}_{\text{act}}$ and the frequency of stochasticity, p. Overlaps of microtubule asters may represent the sites of force generation. We visualized potential overlaps with the motor protein kinesin-5. Kinesin-5 contains four head domains and binds to antiparallel-aligned microtubules. Kinesin-5–GFP labels the spindle during mitosis, as reported previously (46), but also labels the dynamic structures between the microtubule asters in interphases 11–14 (Fig. 7, *a* and *b*). We observed punctuate and sometimes line-like dynamic labeling, which may represent clusters of kinesin-5–GFP at antiparallel-aligned microtubules. We measured the lifetime of these structures with kymographs (Fig. 7 *c*). These measurements show a decline in lifetime with subsequent interphases. For example, in interphase 11, 56% of all measurements measured lifetimes of >20 s, whereas for interphase 14, no lifetime longer

TABLE 1 Model Parameters Identified for Exemplary Data Set and Corresponding Observed and Simulated Order Parameters

		Parameters	Z_0	$\langle \nabla Z(r) \rangle$	$Q_{5,7}$	$g(r_1^*) \times 10^2$
Interphase 11	Simulation	$C = 0.75, p = 0.4$	0.25 ± 0.06	−1.1	1.1 ± 0.3	2.0 ± 0.7
		$C = 0.25, p = 0.5$	0.16 ± 0.04	−1.06	1.1 ± 0.3	2.4 ± 0.7
	Experiment	–	0.13 ± 0.02	−1.41	1.6 ± 0.2	2.7 ± 0.2
Interphase 12	Simulation	$C = 0.75, p = 0.4$	0.18 ± 0.03	−1.1	1.02 ± 0.2	1.8 ± 0.4
	Experiment	–	0.18 ± 0.03	−1.67	1.12 ± 0.09	2.0 ± 0.3
Interphase 13	Simulation	$C = 0.75, p = 0.4$	0.12 ± 0.02	−1.2	1.1 ± 0.2	2.1 ± 0.3
		$C = 1.25, p = 0.2$	0.21 ± 0.03	−1.14	1.0 ± 0.2	1.4 ± 0.2
	Experiment	–	0.24 ± 0.04	−1.60	1.1 ± 0.2	1.4 ± 0.3

To match data for interphase 11 and interphase 13, model parameters C and p from interphase 12 are adjusted each by a factor of about two in opposite ways, yet both times with halved stochasticity. The errors shown result from propagation of uncertainty of SD errors.

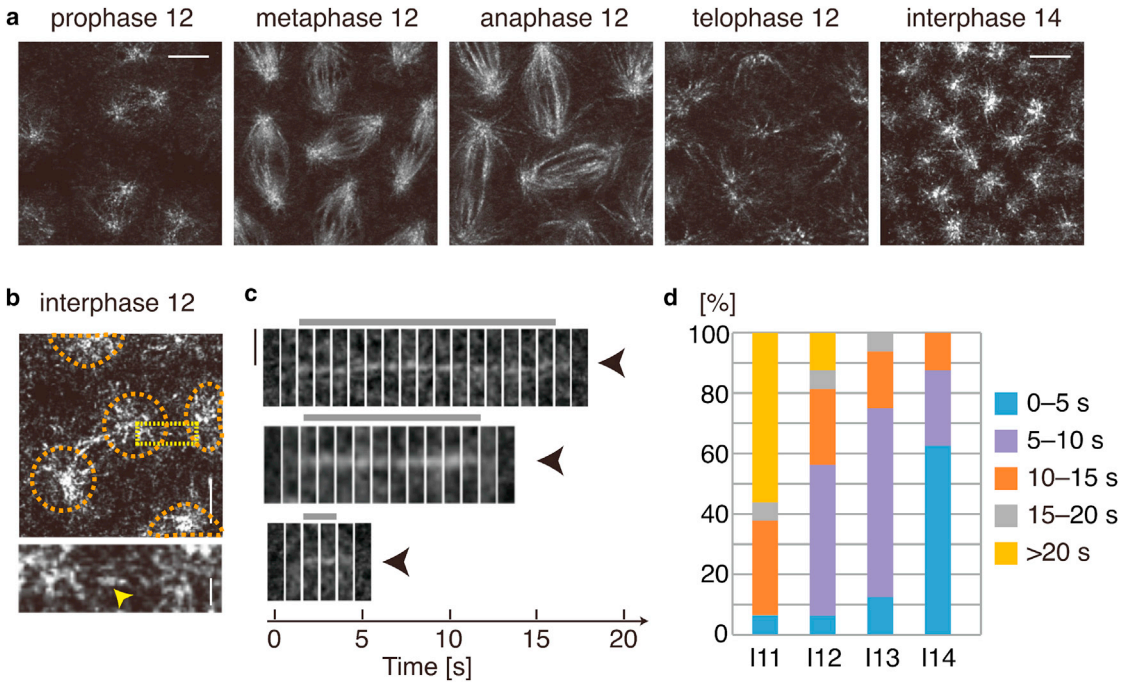

FIGURE 7 (*a*) Live image of *Drosophila* embryo expressing kinesin-5–GFP in different nuclear division phases, as indicated. Scale bars, 5 μm. (*b*) A kinesin-5 cluster associated with centrosomes and in between neighboring nuclei in interphase 12 is shown. Nuclear positions are marked by dashed, orange circles. Scale bars, 5 and 1 μm in the enlarged image. (*c*) A series of snapshots from a time-lapse recording of an embryo expressing kinesin-5–GFP shows the lifetimes of kinesin-5 clusters on microtubule tracks quantified in three examples with varying lifetimes. The arrowheads indicate the kinesin-5 clusters, and the gray bar indicates the lifetime of such a cluster. Scale bars, 2 μm. (*d*) Distribution of kinesin-5 cluster lifetimes are shown over the course of interphases 11, 12, 13, and 14 based on 16 independent lifetime measurements from three different embryos for each interphase. The color code indicates the lifetimes. To see this figure in color, go online.

than 20 s was measured. The majority of measurements, namely 63%, resulted in a lifetime from 0 to 5 s.

Given the abundance in tubulin, microtubule basket overlap is unlikely to be limiting the motor lifetime. The different durations of nuclear cycles cannot be limiting motor lifetime either, as nuclear cycles 10, 11, 12, and 13 last on average longer and longer than 9, 10, 12, and 21 min, respectively (12). Therefore, we assume that indeed kinesin-5 motors do bind for shorter and shorter periods in subsequent interphases. Previous work has shown that kinesin motor lifetime increases in the presence of neighboring motors (47). It is possible that we observe the opposite effect, namely that a reduction in the number of kinesin motors per cluster diminishes a cluster's longevity because of the decrease in cooperative binding (48). Although we cannot resolve a change in kinesin-5 cluster size here, a progressively reducing number of kinesin-5 per cluster over subsequent interphases is consistent with our model's finding of a decreasing stochastic force amplitude C. If less motors act within a given cluster, the amplitude of the stochastic force that they exert goes down. Reduced cluster lifetime with no significant increase in number of clusters, as observed here (see Fig. 7, *a* and *b*), is also consistent with a decrease in the overall percentage of stochastic forces acting, as identified by our model parameter p. Taken together, a reduction of cooperative binding effects of kinesin-5 motors due to a limitation in the number of motors explains both experimental and model observations consistently. This suggest a simple mechanism, where stochastic force is diluted as the amount of kinesin-5 molecules acting per nucleus is approximately halved between subsequent interphases.

DISCUSSION

We investigated how active, stochastic forces due to motor protein activity and passive forces arising from matrix-mediated interaction organize nuclear arrangement in syncytial cells. We presented and analyzed a mechanical model of nuclear ordering by including these two forces as main ingredients. Numerically investigating the model and quantifying the observed nuclear order of the model predicts a decrease of order when solely doubling nuclear density upon nuclear division. By comparing model results to recordings of nuclear arrangements in *Drosophila* embryos, we make contradictory observations of increasing order after nuclear divisions, which we capture within our model by reducing stochasticity in the relevant parameters upon every round of nuclear division. Measurement of decreasing kinesin-5 cluster lifetime supports the decrease in stochastic forces. We therefore deduce that limited motor protein activity is buffering a potential increase in stochasticity because of mitosis.

To model nuclear dynamics during interphase in *Drosophila*, we combined active, stochastic forces with the passive interaction forces arising from circular inclusions, representing the nuclei, within an elastic matrix. The latter model has previously only been applied to describe entire cells on gel substrate (25–27). The success of our theoretical model in the given context suggests that the framework may also well extend beyond isolated cells to adherent cells forming tissue. The framework of inclusions within an elastic matrix is very rich and can, for example, be extended to different inclusion shapes (25) and feedback between cells and matrix, leading to self-polarization of cells (31). Furthermore, we show that stochastic forces can well be included in this model framework, allowing capture of fluctuations presumably not only in nuclei but also in cell arrangements.

We quantified nuclear arrangements during interphase with spatial and orientational order parameters. Our analysis suggests that the system is in a liquid-like state, as measured by the exponential decay of the hexagonal order parameter (Eq. 4) and the corresponding intermediate values of the radial distribution at the first minimum. Note that our analysis for hyperuniformity indicates non-hyperuniformity for nuclei arrangements (see Fig. S1). This behavior is expected because of the free-flowing nature of the nuclei within the common cytoplasm. We note the importance of stochastic forces for the arrangement of nuclei, corresponding to the arrangement of particles in fluid phase with only a certain degree of order.

By modeling stochastic interactions, we make use of a constant motor processivity time and instead vary the time-averaged overall activity of stochastic forces to be able to easily tune the parameters in simulations; this is, however, a simplification. In reality, the processivity time varies even within one interphase and thus would have to be drawn from a distribution that we, at the present point, cannot access. To test different types of distributions and quantify their effect on the results presented here would be an interesting extension of our model.

Whereas active, stochastic forces play an eminent role in the nuclear arrangements, we find that their strength is tamed over the course of mitotic cycles. The required twofold decrease in model parameters corresponding to stochasticity in our simulations is shown to go hand-in-hand with a decrease in lifetime of kinesin-5 clusters. Thus, likely stochastic forces decrease as the number of kinesin-5 motor proteins per nucleus, known to guide nuclear interaction, is diluted in subsequent interphases. The rapidness of mitotic cycles may not allow for the production of motor proteins to keep up with the amount of nuclei, thereby limiting active interaction between nuclei. Diluting motor proteins and thereby taming stochastic forces to achieve ordered nuclear arrangements may be a very simple and, at the same time, powerful mechanism to self-organize embryogenesis, which is a concept simple enough to be well applicable beyond the syncytial embryos of *Drosophila*.

SUPPORTING MATERIAL

Supporting Materials and Methods and three figures are available at http://www.biophysj.org/biophysj/supplemental/S0006-3495(18)30249-2.

AUTHOR CONTRIBUTIONS

F.K. and K.A. designed the research. F.K. performed the theoretical and numerical analysis. J.G. designed the experiments. Z.L. and D.M.R. conducted the experiments and collected data. J.R. and T.A. segmented and analysed image data. F.K., Z.L., J.G., and K.A. wrote the manuscript.

ACKNOWLEDGMENTS

The authors gratefully acknowledge Annette Zippelius and Stephan Ulrich for their prerequisite work and ideas, which made this publication possible.

This work was in part supported by the Göttingen Centre for Molecular Biology (funds for equipment repair), the Max Planck Society, and the Deutsche Forschungsgemeinschaft via grants SFB-937/A19 (K.A.), SFB-937/A10 (T.A. and J.G.), and INST1525/16-1 FUGG (J.G.).

REFERENCES

1. Camazine, S., N. R. Franks, …, G. Theraulaz. 2001. Self-Organization in Biological Systems. Princeton University Press, Princeton, NJ.
2. Turing, A. M. 1952. The chemical basis of morphogenesis. *Philos. Trans. R. Soc. Lond. B Biol. Sci.* 237:37–72.
3. Koch, A. J., and H. Meinhardt. 1994. Biological pattern formation: from basic mechanisms to complex structures. *Rev. Mod. Phys.* 66: 1481–1507.
4. Cross, M. C., and P. C. Hohenberg. 1993. Pattern formation outside of equilibrium. *Rev. Mod. Phys.* 65:851–1112.
5. Karsenti, E. 2008. Self-organization in cell biology: a brief history. *Nat. Rev. Mol. Cell Biol.* 9:255–262.
6. Alberts, B., A. Johnson, …, P. Walter. 2002. Molecular Biology of the Cell, Fourth Edition. Garland Science, New York.
7. Rodriguez, O. C., A. W. Schaefer, …, C. M. Waterman-Storer. 2003. Conserved microtubule-actin interactions in cell movement and morphogenesis. *Nat. Cell Biol.* 5:599–609.
8. Munjal, A., and T. Lecuit. 2014. Actomyosin networks and tissue morphogenesis. *Development*. 141:1789–1793.
9. Murrell, M., P. W. Oakes, …, M. L. Gardel. 2015. Forcing cells into shape: the mechanics of actomyosin contractility. *Nat. Rev. Mol. Cell Biol.* 16:486–498.
10. Heisenberg, C. P., and Y. Bellaïche. 2013. Forces in tissue morphogenesis and patterning. *Cell*. 153:948–962.
11. Kanesaki, T., C. M. Edwards, …, J. Grosshans. 2011. Dynamic ordering of nuclei in syncytial embryos: a quantitative analysis of the role of cytoskeletal networks. *Integr. Biol.* 3:1112–1119.
12. Foe, V. E., and B. M. Alberts. 1983. Studies of nuclear and cytoplasmic behaviour during the five mitotic cycles that precede gastrulation in *Drosophila* embryogenesis. *J. Cell Sci.* 61:31–70.
13. Karr, T. L., and B. M. Alberts. 1986. Organization of the cytoskeleton in early *Drosophila* embryos. *J. Cell Biol.* 102:1494–1509.
14. Winkler, F., M. Gummalla, …, J. Grosshans. 2015. Fluctuation analysis of centrosomes reveals a cortical function of *kinesin-1*. *Biophys. J.* 109: 856–868.
15. Koke, C., T. Kanesaki, …, C. M. Dunlop. 2014. A computational model of nuclear self-organisation in syncytial embryos. *J. Theor. Biol.* 359:92–100.
16. Schejter, E. D., and E. Wieschaus. 1993. Functional elements of the cytoskeleton in the early *Drosophila* embryo. *Annu. Rev. Cell Biol.* 9:67–99.

17. Foe, V. E., and G. Odell. 1993. Mitosis and morphogenesis in the Drosophila embryo: point and counterpoint. *In* The Development of Drosophila Melanogaster. M. Bate and A. M. Arias, eds. Cold Spring Harbor Laboratory Press, pp. 149–300.
18. Foe, V. E., C. M. Field, and G. M. Odell. 2000. Microtubules and mitotic cycle phase modulate spatiotemporal distributions of F-actin and myosin II in *Drosophila* syncytial blastoderm embryos. *Development*. 127:1767–1787.
19. Cao, J., J. Crest, …, W. Sullivan. 2010. Cortical actin dynamics facilitate early-stage centrosome separation. *Curr. Biol.* 20:770–776.
20. Scholey, J. M. 2009. *Kinesin-5* in *Drosophila* embryo mitosis: sliding filament or spindle matrix mechanism? *Cell Motil. Cytoskeleton*. 66:500–508.
21. Hoffman, B. D., and J. C. Crocker. 2009. Cell mechanics: dissecting the physical responses of cells to force. *Annu. Rev. Biomed. Eng.* 11:259–288.
22. Idema, T., J. O. Dubuis, …, A. J. Liu. 2013. The syncytial *Drosophila* embryo as a mechanically excitable medium. *PLoS One*. 8:e77216.
23. Deneke, V. E., A. Melbinger, …, S. Di Talia. 2016. Waves of *Cdk1* activity in S phase synchronize the cell cycle in *Drosophila* embryos. *Dev. Cell*. 38:399–412.
24. Schwarz, U. S., and S. A. Safran. 2002. Elastic interactions of cells. *Phys. Rev. Lett.* 88:048102.
25. De, R., A. Zemel, and S. A. Safran. 2007. Dynamics of cell orientation. *Nat. Phys.* 3:655–659.
26. Yuval, J., and S. A. Safran. 2013. Dynamics of elastic interactions in soft and biological matter. *Phys. Rev. E Stat. Nonlin. Soft Matter Phys.* 87:042703.
27. Puljiz, M., and A. M. Menzel. 2017. Forces and torques on rigid inclusions in an elastic environment: resulting matrix-mediated interactions, displacements, and rotations. *Phys. Rev. E.* 95:053002.
28. Bischofs, I. B., S. A. Safran, and U. S. Schwarz. 2004. Elastic interactions of active cells with soft materials. *Phys. Rev. E Stat. Nonlin. Soft Matter Phys.* 69:021911.
29. Landau, L., and E. Lifshitz. 1986. Theory of Elasticity, Third Edition. Butterworth-Heinemann, Oxford, UK.
30. Kapitein, L. C., E. J. Peterman, …, C. F. Schmidt. 2005. The bipolar mitotic *kinesin Eg5* moves on both microtubules that it crosslinks. *Nature*. 435:114–118.
31. Zemel, A., F. Rehfeldt, …, S. A. Safran. 2010. Optimal matrix rigidity for stress fiber polarization in stem cells. *Nat. Phys.* 6:468–473.
32. Wessel, A. D., M. Gumalla, …, C. F. Schmidt. 2015. The mechanical properties of early *Drosophila* embryos measured by high-speed video microrheology. *Biophys. J.* 108:1899–1907.
33. Tomer, R., K. Khairy, …, P. J. Keller. 2012. Quantitative high-speed imaging of entire developing embryos with simultaneous multiview light-sheet microscopy. *Nat. Methods*. 9:755–763.
34. Halperin, B. I., and D. R. Nelson. 1978. Theory of two-dimensional melting. *Phys. Rev. Lett.* 41:121–124.
35. Zippelius, A., B. I. Halperin, and D. R. Nelson. 1980. Dynamics of two-dimensional melting. *Phys. Rev. B*. 22:2514–2541.
36. Nelson, D. R., and B. I. Halperin. 1979. Dislocation-mediated melting in two dimensions. *Phys. Rev. B*. 19:2457–2484.
37. Farhadifar, R., J. C. Röper, …, F. Jülicher. 2007. The influence of cell mechanics, cell-cell interactions, and proliferation on epithelial packing. *Curr. Biol.* 17:2095–2104.
38. Hočevar, A., and P. Ziherl. 2009. Degenerate polygonal tilings in simple animal tissues. *Phys. Rev. E Stat. Nonlin. Soft Matter Phys.* 80:011904.
39. Chandler, D. 1987. Introduction to Modern Statistical Mechanics. Oxford University Press, Oxford, UK.
40. Torquato, S., and F. H. Stillinger. 2003. Local density fluctuations, hyperuniformity, and order metrics. *Phys. Rev. E Stat. Nonlin. Soft Matter Phys.* 68:041113.
41. Chen, D., W. Y. Aw, …, S. Torquato. 2016. Structural characterization and statistical-mechanical model of epidermal patterns. *Biophys. J.* 111:2534–2545.
42. Gramates, L. S., S. J. Marygold, …, P. Zhou; the FlyBase Consortium. 2017. FlyBase at 25: looking to the future. *Nucleic Acids Res.* 45:D663–D671.
43. Lv, Z., J. Rosenbaum, …, J. Großhans. 2018. A 'molecular guillotine' reveals the interphase function of *kinesin-5*. *J. Cell. Sci.* 131:jcs210583.
44. Schindelin, J., I. Arganda-Carreras, …, A. Cardona. 2012. Fiji: an open-source platform for biological-image analysis. *Nat. Methods*. 9:676–682.
45. Lindeberg, T. 1998. Feature detection with automatic scale selection. *Int. J. Comput. Vis.* 30:79–116.
46. Cheerambathur, D. K., I. Brust-Mascher, …, J. M. Scholey. 2008. Dynamic partitioning of mitotic *kinesin-5* cross-linkers between microtubule-bound and freely diffusing states. *J. Cell Biol.* 182:429–436.
47. Roos, W. H., O. Campàs, …, G. Cappello. 2008. Dynamic kinesin-1 clustering on microtubules due to mutually attractive interactions. *Phys. Biol.* 5:046004.
48. Muto, E., H. Sakai, and K. Kaseda. 2005. Long-range cooperative binding of *kinesin* to a microtubule in the presence of ATP. *J. Cell Biol.* 168:691–696.